

AM-FM: A Foundation Model for Ambient Intelligence Through WiFi

Guozhen Zhu¹ Yuqian Hu¹ Sakila Jayaweera¹ Weihang Gao¹ Wei-Hsiang Wang¹ Jiaxuan Zhang¹
Beibei Wang¹ Chenshu Wu^{1,2} K. J. Ray Liu¹

Abstract

Ambient intelligence, continuously understanding human presence, activity, and physiology in physical spaces, is fundamental to smart environments, health monitoring, and human-computer interaction. WiFi infrastructure provides a ubiquitous, always-on, privacy-preserving substrate for this capability across billions of IoT devices. Yet this potential remains largely untapped, as wireless sensing has typically relied on task-specific models that require substantial labeled data and limit practical deployment. We present AM-FM, the first foundation model for ambient intelligence and sensing through WiFi. AM-FM is pre-trained on 9.2 million unlabeled Channel State Information (CSI) samples collected over 439 days from 20 commercial device types deployed worldwide, learning general-purpose representations via contrastive learning, masked reconstruction, and physics-informed objectives tailored to wireless signals. Evaluated on public benchmarks spanning nine downstream tasks, AM-FM shows strong cross-task performance with improved data efficiency, demonstrating that foundation models can enable scalable ambient intelligence using existing wireless infrastructure.

1. Introduction

Ambient intelligence that continuously senses and responds to its occupants underpins applications from smart home automation to elderly care and occupational health monitoring. Realizing this vision requires perception that is always-on, unobtrusive, and deployable at scale. WiFi signals offer a compelling substrate for ambient perception. They propagate through walls, function in any lighting condition, require no contact or worn devices, and preserve visual privacy. The billions of access points, smart speakers,

¹Origin Research, Rockville, USA ²The University of Hong Kong, Hong Kong, China. Correspondence to: Guozhen Zhu <gzzhu@terpmail.umd.edu>.

Preprint. February 13, 2026.

and IoT devices already deployed continuously transmit signals that interact with the environment and its occupants, and their channel state information (CSI) captures motion patterns as well as subtle physiological signals such as respiration. This ubiquitous wireless substrate could enable ambient perception at unprecedented scale without additional infrastructure.

Despite this potential, wireless sensing research has predominantly relied on task-specific models trained from scratch for individual applications. Each new task or sensing scenario requires designing custom architectures, collecting labeled data, and training specialized models. This fragmentation limits practical deployment: substantial labeled data is needed for every task and setting, and knowledge cannot be shared across the diverse sensing capabilities that WiFi infrastructure enables.

Foundation models have demonstrated that large-scale self-supervised pre-training on diverse data produces general-purpose representations that transfer effectively across tasks and domains. Drawing from the success of foundation models in natural language processing and computer vision, we explore whether this paradigm extends to ambient perception. WiFi presents a compelling opportunity for this approach: commodity hardware already generates massive streams of unlabeled CSI data; a single pre-trained backbone can serve applications from coarse spatial reasoning to fine-grained physiological monitoring; and WiFi signals penetrate walls, enabling ambient sensing in conditions where other modalities struggle.

However, extending foundation models to WiFi sensing presents unique technical challenges. CSI exhibits non-local frequency structure arising from multipath propagation, which is distinct from the spatial locality observed in images or the spectral smoothness characteristic of audio signals. Subcarriers have heterogeneous signal quality depending on hardware, interference, and propagation conditions, requiring adaptive processing across the frequency dimension. Human activities induce characteristic patterns that benefit from translation-invariant temporal modeling. Additionally, the modality lacks established large-scale pre-training datasets, and standard self-supervised objectives designed for vision or language may not capture the physics

of wireless signal propagation.

In this paper, we present AM-FM, to our knowledge the first Foundation Model for AMbient intelligence based on WiFi sensing. We pre-train on 9.2 million unlabeled CSI data continuously collected in 439 days with 20 commercial device types across 8 chipset families, 11 real-world environments, and 26 users, capturing diverse hardware characteristics, environmental conditions, and human activities. AM-FM employs a self-supervised learning framework combining contrastive objectives, masked reconstruction, and physics-informed autocorrelation prediction, tailored to the spatiotemporal structure of CSI. The architecture incorporates adaptive frequency aggregation to handle heterogeneous subcarrier quality and relative temporal encoding to capture translation-invariant patterns. We evaluate on public benchmarks spanning nine downstream tasks through parameter-efficient fine-tuning.

Our key contributions include: 1) **Developing a foundation model for ambient intelligence**: We outline the design and development of the first large-scale foundation model for ambient intelligence with WiFi sensing. 2) **Domain-specific pre-training with large-scale real-world dataset**: We show that with a large-scale unlabeled WiFi dataset, a self-supervised learning framework tailored to the characteristics of wireless signals can extract representations for practical ambient perception. 3) **Strong performance of single backbone on diverse tasks with superior data efficiency**: We demonstrate AM-FM’s generalizability and real-world utility across nine diverse WiFi sensing tasks from public benchmarks, establishing that the foundation model paradigm extends successfully to WiFi-based ambient perception.

2. Related Work

Foundation models for perception. Foundation models have transformed representation learning across perceptual domains by enabling transfer from large-scale unlabeled data. In vision, masked autoencoders and contrastive learning produce transferable representations under limited supervision (He et al., 2022; Radford et al., 2021). This paradigm has extended to other sensing modalities: wav2vec 2.0 dramatically improves sample efficiency in speech recognition (Baevski et al., 2020), and recent work in inertial sensing demonstrates cross-user and cross-device transfer using pre-trained models (Xu et al., 2021). A consistent finding is that foundation models not only reduce labeling requirements, but also enable knowledge sharing across tasks within a modality. Despite these successes across vision, language, audio, and inertial sensing, WiFi-based ambient perception has yet to be explored through the foundation model lens.

WiFi for ambient perception. WiFi Channel State Information (CSI) captures how radio signals propagate through indoor environments, where multipath reflections from static structures and human motion produce characteristic spatiotemporal variations. This property enables diverse applications including activity recognition (Wang et al., 2015; Miao et al., 2025), gesture detection (Abdelnasser et al., 2015b; Zhao et al., 2024), respiration monitoring (Abdelnasser et al., 2015a; Guo et al., 2023), and indoor localization (Kotaru et al., 2015; Wang et al., 2024). WiFi signals propagate through walls, operate independently of lighting conditions, require no wearable devices, and leverage billions of already deployed access points and IoT devices, thereby enabling continuous and unobtrusive perception using existing infrastructure. These characteristics make WiFi particularly suitable for ambient intelligence applications in homes, offices, and healthcare settings.

Task-specific WiFi sensing approaches. Current WiFi sensing research has primarily focused on developing specialized models for individual applications. Most systems are designed and trained from scratch for specific tasks such as activity recognition (Wang et al., 2015; Miao et al., 2025), fall detection (Chu et al., 2023), or localization (Zhou et al., 2017; Wang et al., 2024), using task-specific architectures and supervised learning on labeled datasets. While these approaches have demonstrated the feasibility of WiFi sensing across various applications, each new task typically requires collecting labeled data and designing custom models. Some prior efforts explore domain adaptation (Zhang et al., 2018), adversarial learning (Wang et al., 2021), and physics-driven feature engineering (Zheng et al., 2019) to improve model transferability, but these are task-specific solutions rather than general-purpose representation learning frameworks. The question of whether a single pre-trained model can effectively support multiple WiFi sensing tasks, analogous to foundation models in vision and language, remains largely unexplored.

Self-supervised learning for wireless signals. Self-supervised learning (SSL) offers a pathway toward learning from unlabeled data by exploiting inherent structure. Contrastive objectives encourage invariance to appropriate transformations (Chen et al., 2020; He et al., 2020), while masked prediction captures local and global patterns (He et al., 2022). SSL has been widely adopted across a variety of wireless sensing applications and has demonstrated improved sample efficiency and achieved performance comparable to supervised learning under same-domain settings across a range of wireless sensing tasks; however, existing efforts are predominantly confined to specific sensing tasks and narrowly scoped datasets, with limited diversity in devices and environments (Radwan et al., 2026). Moreover, for WiFi sensing specifically, despite the abundance of unlabeled CSI continuously generated by deployed infras-

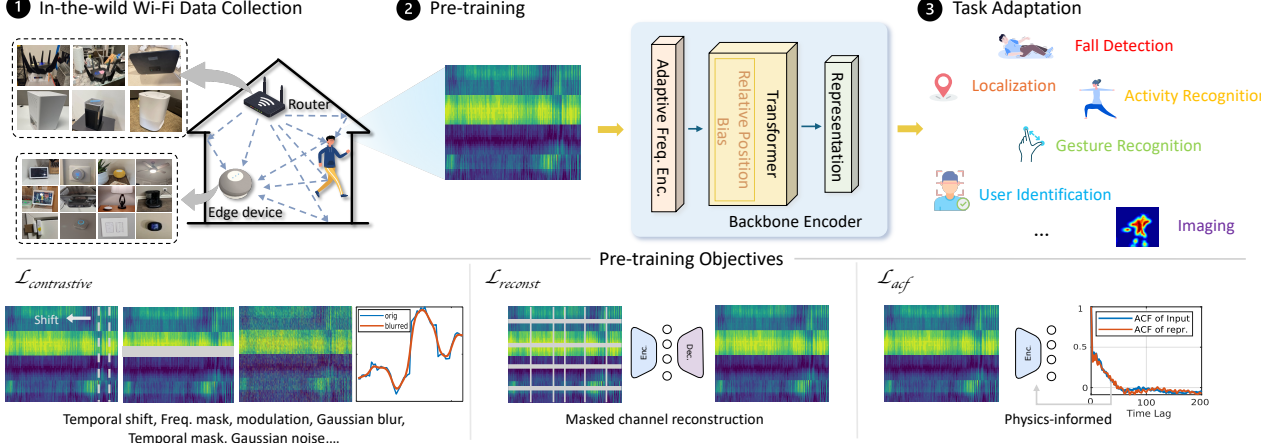


Figure 1. AM-FM Framework. (Left) Continuous CSI collection from distributed IoT devices. (Center) Self-supervised pre-training with contrastive learning, masked reconstruction, and physics-informed ACF prediction. (Right) Parameter-efficient adaptation to downstream tasks via lightweight temporal classifiers or bottleneck adapters.

tructure, no prior work has established a large-scale, diverse pre-training dataset nor has it systematically investigated whether foundation model pre-training enables effective transfer across the wide range of sensing tasks WiFi supports. Existing benchmarks like CSI-Bench (Zhu et al., 2025a) provide valuable labeled evaluation data spanning multiple devices and environments, but are designed for supervised evaluation rather than self-supervised pre-training. Furthermore, CSI exhibits unique structural properties, including non-local frequency dependencies induced by multipath propagation, heterogeneous subcarrier quality, and periodic temporal patterns associated with human activities (Brunello et al., 2025), which require domain-informed self-supervised learning objectives beyond those commonly used in vision or audio.

Our work addresses this gap by introducing AM-FM, the first foundation model for WiFi-based ambient perception. We construct a diverse pre-training dataset and design self-supervised objectives tailored to wireless signal characteristics. The results demonstrate that the foundation model paradigm extends effectively to ambient perception via WiFi.

3. Data

Foundation models derive their power from learning on diverse, large-scale data that captures the natural variation of target domains. We collect a pre-training dataset that reflects the heterogeneity inherent in real-world ambient intelligence system deployments.

3.1. Pre-training dataset

We collect an in-the-wild WiFi CSI dataset comprising over 439 days of continuous CSI recordings (~ 20 TB with over 9.2 million data samples) from 20 commercial IoT device types deployed across 11 real-world environments with 26 participants. The dataset includes multiple physical instances per device type (33 devices in total), introducing intra-type device diversity. To our knowledge, this constitutes the largest and most diverse WiFi sensing dataset collected to date for foundation model pre-training.

The dataset spans 8 chipset families (MediaTek, Qualcomm, Broadcom, Espressif, NXP, Marvell, Realtek, Alttobeam) with antenna configurations from 1×1 to 2×2 MIMO, channel bandwidths of 20/40/80 MHz across 2.4 and 5 GHz bands, and received power difference can exceed 20 dB across devices and configurations (more details in Appendix B.2 Table 4). This heterogeneity reflects the fragmented hardware ecosystem of real-world deployments, where applications must generalize across diverse commodity devices.

Environments include studios, apartments, houses, and townhouses ranging from 576–3,800 sq ft with 1–3 floors (more details in Appendix B.3 Table 5). Each deployment differs in layout, furniture density, device placement, and interference conditions, producing diverse multipath propagation patterns that challenge environment-specific models.

CSI is recorded continuously (24/7) during natural daily activities with 6–9 concurrent distributed device links per environment. This in-the-wild collection captures realistic motion, occlusions, and interference, reflecting real-world deployment conditions beyond scripted laboratory settings.

The fragmentation of existing WiFi sensing approaches

stems partly from reliance on small, homogeneous datasets that fail to capture cross-device and cross-environment variation (Wang et al., 2025). By pre-training on data that spans this variation, our foundation model learns representations that transfer across the heterogeneous conditions encountered in practice.

3.2. WiFi CSI: Structure and Properties

CSI describes how wireless signals propagate between transmitter and receiver, encoding the amplitude and phase response across frequency subcarriers. When objects move within the propagation environment, they modulate these channel responses in ways that can be decoded for sensing applications (Ma et al., 2019).

Three structural properties of CSI motivate our architectural design choices. First, CSI exhibits non-local frequency structure: due to multipath propagation, environmental changes induce structured and environment-dependent correlations across subcarriers. Unlike the spatial locality in images or the smooth spectral structure in audio, subcarrier relationships in CSI are not governed by fixed local neighborhoods; correlations may emerge between distant frequency components depending on the propagation geometry. This observation suggests that frequency modeling for CSI should be adaptive, rather than relying on fixed locality assumptions inherited from vision or audio domains (Ahmad et al., 2024).

Second, subcarriers exhibit heterogeneous signal quality due to hardware characteristics, interference conditions, and propagation geometry. Some subcarriers may be dominated by noise while others reliably capture motion-induced variations. Therefore, effective representations should learn to weight subcarriers by their information content rather than treating all frequencies equally (Zhang et al., 2021; Ahmad et al., 2024).

Third, human activities induce characteristic periodic patterns across different timescales: respiration at 0.2–0.5 Hz, gait at 1–2 Hz, and gestures at 2–5 Hz. These periodicities are translation-invariant. The same activity produces similar patterns regardless of when it occurs, motivating temporal modeling that captures relative rather than absolute timing (Tao et al., 2025; Su et al., 2026).

3.3. Data Preprocessing

We design a unified preprocessing pipeline that converts raw CSI from heterogeneous devices into a standardized representation suitable for foundation model pre-training, without relying on task-specific heuristics that would limit generalization.

Raw CSI is parsed into a complex-valued tensor $\mathbf{H} \in \mathbb{C}^{N_{\text{tx}} \times N_{\text{rx}} \times N_{\text{sub}} \times T}$, where $N_{\text{tx}}, N_{\text{rx}}$ denote antenna counts,

N_{sub} is the number of subcarriers, varying with channel bandwidth, and T is temporal length. We flatten spatial-frequency dimensions to $\mathbf{X} \in \mathbb{C}^{F \times T}$ with $F = N_{\text{tx}}N_{\text{rx}}N_{\text{sub}}$, preserving the full information content while enabling uniform processing.

CSI streams are collected with a target packet rate of 100 Hz, but effective rates vary across devices due to hardware and environmental factors. We estimate effective rates from inter-packet timestamps and discard streams falling below two-thirds of the target rate to ensure sufficient temporal resolution for motion sensing.

We extract CSI amplitude $\mathbf{A} = |\mathbf{X}|$, which is robust to the phase noise common in commodity hardware (Xie et al., 2019). Continuous streams are segmented into non-overlapping fixed-length windows, producing segments $\mathbf{S}_i \in \mathbb{R}^{L \times F}$, where L is the number of samples per window. No task-driven segmentation or filtering is applied, preserving generality for diverse downstream applications.

To handle heterogeneous WiFi devices with varying subcarrier and antenna configurations, all CSI segments are zero-padded to a unified frequency–spatial dimension F_{max} , defined by the maximum feature size observed across devices. Segments are normalized to $[0, 1]$ using per-segment min–max normalization and stored in compressed HDF5 format.

4. Foundation Model Development

We present a self-supervised framework for learning transferable WiFi CSI representations. Our design choices are guided by the structural properties of CSI identified in Section 3.2, with the goal of learning representations that generalize across a wide variety of sensing tasks.

4.1. Architecture

The encoder transforms raw CSI segments into compact representations through two key mechanisms: adaptive frequency aggregation that handles heterogeneous signal quality, and relative temporal encoding that captures translation-invariant activity patterns.

To handle variable subcarrier quality across devices and environments, we employ cross-attention that compresses F input subcarriers into $F' = 10$ latent frequency channels:

$$\begin{aligned} \mathbf{z}_t &= \sum_{f=1}^F \alpha_{tf} (\mathbf{W}_v \mathbf{x}_{tf} + \mathbf{p}_f), \\ \alpha_{tf} &= \text{softmax}_f \left(\frac{\mathbf{q}^\top (\mathbf{W}_k \mathbf{x}_{tf} + \mathbf{p}_f)}{\sqrt{d}} \right), \end{aligned} \quad (1)$$

where $\mathbf{q} \in \mathbb{R}^{F' \times d}$ are learnable queries and \mathbf{p}_f denotes sinusoidal frequency encodings. This achieves 5–11 × com-

pression through learning to weight subcarriers by their information content, addressing the heterogeneous signal quality property discussed in Section 3.2.

To capture translation-invariant temporal patterns characteristic of human activities, we use relative position bias in self-attention:

$$\text{Attn}_{ij} = \text{softmax} \left(\frac{\mathbf{q}_i^\top \mathbf{k}_j}{\sqrt{d_k}} + b_{ij} \right) \mathbf{v}_j, \quad b_{ij} = f_\theta(j - i), \quad (2)$$

where f_θ learns embeddings over relative temporal distances. This design enables the model to recognize that the same activity pattern—whether respiration, gait, or gesture—produces similar representations regardless of when it occurs in the input window.

The encoder consists of adaptive frequency aggregation followed by a 6-layer transformer with hidden dimension $d = 256$ and 8 attention heads. A 3-layer decoder handles reconstruction during pre-training. We refer to this configuration as the Base model (5M parameters); we also explore Small (2M) and Large (12M) variants in Section 5.4 to study scaling behavior.

4.2. Self-Supervised Learning Framework

We combine three complementary objectives that capture distinct structural properties of CSI as shown in Figure 1, enabling the model to learn representations useful for diverse downstream tasks without labeled data.

The first objective is contrastive learning. Given augmented views $\mathbf{x}_1, \mathbf{x}_2$ of input \mathbf{x} , we obtain temporal-pooled representations $\mathbf{z}_1, \mathbf{z}_2 \in \mathbb{R}^d$ and apply the NT-Xent loss:

$$\mathcal{L}_{\text{CL}} = -\frac{1}{2B} \sum_{i=1}^{2B} \log \frac{\exp(\text{sim}(\mathbf{p}_i, \mathbf{p}_{j(i)})/\tau)}{\sum_{k=1}^{2B} \exp(\text{sim}(\mathbf{p}_i, \mathbf{p}_k)/\tau)}, \quad (3)$$

where $\mathbf{p} = g(\mathbf{z})$ is an MLP projection, $j(i)$ denotes the positive pair, and $\tau = 0.2$. This objective encourages representations that capture semantic activity content while remaining invariant to nuisance variations in channel conditions.

CSI data is sensitive to channel conditions, device variation, and acquisition artifacts. We apply nine domain-informed augmentations that simulate realistic perturbations while preserving activity semantics: additive Gaussian noise simulates low-SNR conditions; amplitude modulation emulates Automatic Gain Control variation and path loss; temporal shift creates circular misalignment; frequency perturbation introduces mild spectral distortions; temporal crop simulates truncated or compressed actions; frequency masking forces reliance on distributed spectral cues; and Gaussian blur smooths high-frequency fluctuations. Each view is independently augmented by randomly sampling a subset of

these transformations, promoting robustness to hardware and environmental variability.

The second objective is masked reconstruction. We randomly mask 10% of temporal blocks and 10% of frequency bands, simulating packet loss and selective fading common in wireless systems. A reconstruction head predicts the original unmasked signal:

$$\mathcal{L}_{\text{REC}} = \|\hat{\mathbf{X}} - \mathbf{X}\|_2^2. \quad (4)$$

Unlike masked autoencoders that reconstruct only masked regions, we reconstruct the entire signal, forcing the model to learn the spatial-temporal coherence and cross-frequency correlations arising from multipath propagation.

The third objective is physics-informed prediction. The autocorrelation function (ACF) measures the temporal self-correlation of CSI power, which increases under continuous motion due to coherent channel variations, and has been explored in statistically-based WiFi sensing methods (Zhang et al., 2019) to capture human movement in space. We introduce an auxiliary task that predicts the normalized ACF of the signal energy over time. Given $s_t = \mathbb{E}_f[\mathbf{X}_{tf}^2]$, the ACF is:

$$\text{ACF}[k] = \frac{\sum_{t=0}^{T-k-1} s_t s_{t+k}}{\sum_{t=0}^{T-1} s_t^2}, \quad (5)$$

computed efficiently via FFT. An MLP head regresses the first $K = 50$ lags:

$$\mathcal{L}_{\text{ACF}} = \|\widehat{\text{ACF}} - \text{ACF}(\mathbf{X})\|_2^2. \quad (6)$$

This physics-informed objective encourages the encoder to learn representations sensitive to the rhythmic temporal structure characteristic of human activities.

The overall training objective combines all three losses:

$$\mathcal{L} = \lambda_{\text{CL}} \mathcal{L}_{\text{CL}} + \lambda_{\text{REC}} \mathcal{L}_{\text{REC}} + \lambda_{\text{ACF}} \mathcal{L}_{\text{ACF}}, \quad (7)$$

with $\lambda_{\text{CL}} = 1$, $\lambda_{\text{REC}} = 4$, and $\lambda_{\text{ACF}} = 3$.

4.3. Pre-training Details

We optimize using AdamW with learning rate 10^{-4} and weight decay 10^{-4} , employing linear warmup over 10 epochs followed by cosine annealing. Training uses mixed-precision (FP16) on 8 A100 GPUs with effective batch size 256. Gradient clipping (max norm 1.0) and numerical stabilization ensure stable training. Pre-training converges within 200 epochs.

4.4. Downstream Adaptation

A key advantage of foundation models is efficient adaptation to new tasks with minimal labeled data. We evaluate two adaptation strategies that span the efficiency–flexibility tradeoff.

Table 1. Cross-task performance across downstream WiFi sensing tasks. AUROC and 95% confidence intervals (CI) are reported for classification tasks and SSIM / PSNR are reported for the reconstruction task Imaging[†].

Method	Fall	HAR	Gesture	UID	Localization	MSR	Occupancy	Proximity	Imaging [†]
AM-FM + BA	0.919 (0.902, 0.935)	0.923 (0.915, 0.932)	0.999 (0.999, 0.999)	0.993 (0.990, 0.995)	0.995 (0.992, 0.997)	0.974 (0.970, 0.977)	0.989 (0.986, 0.992)	0.936 (0.927, 0.946)	0.726 / 18.87
AM-FM + TP	0.873 (0.851, 0.893)	0.915 (0.906, 0.922)	0.634 (0.623, 0.645)	0.996 (0.994, 0.997)	0.990 (0.986, 0.994)	0.992 (0.991, 0.993)	0.989 (0.985, 0.992)	0.928 (0.919, 0.938)	0.722 / 18.43
Scratch	0.916 (0.899, 0.932)	0.527 (0.513, 0.541)	0.564 (0.562, 0.568)	0.995 (0.993, 0.997)	0.631 (0.606, 0.653)	0.593 (0.581, 0.606)	0.566 (0.544, 0.587)	0.494 (0.477, 0.510)	0.726 / 18.41

Temporal Probing. The simplest adaptation strategy freezes all encoder parameters and trains only a lightweight classifier on the sequence of frame representations. As wireless sensing depends on temporal dynamics that pooling would discard, we employ a temporal classifier with a single-layer LSTM:

$$\hat{y} = g_\phi(\text{LSTM}(\mathbf{z}_1, \mathbf{z}_2, \dots, \mathbf{z}_T)), \quad (8)$$

where $\mathbf{z}_t \in \mathbb{R}^d$ are the frozen encoder outputs and g_ϕ is a classification head. This approach tests whether pre-trained representations encode useful structure for downstream tasks without any encoder adaptation.

Bottleneck Adaptation. For tasks requiring more expressive adaptation, we inject lightweight adapter modules into each transformer layer while keeping pre-trained weights frozen:

$$\mathcal{A}_l(\mathbf{h}) = \mathbf{W}_{\text{up}}^{(l)} \cdot \text{GELU} \left(\mathbf{W}_{\text{down}}^{(l)} \cdot \mathbf{h} \right), \quad (9)$$

where $\mathbf{W}_{\text{down}}^{(l)} \in \mathbb{R}^{r \times d}$ projects to bottleneck dimension r , and $\mathbf{W}_{\text{up}}^{(l)} \in \mathbb{R}^{d \times r}$ projects back. The adapter output combines with frozen layer outputs via residual connection. We initialize \mathbf{W}_{up} to zero, ensuring identical outputs to the pre-trained encoder at initialization. With $d = 192$, $r = 192$, and $L = 6$ layers, adapters add approximately 393K parameters—less than 3% of the encoder. Both adaptation methods use the same temporal classifier, isolating the effect of adapter tuning.

All methods use AdamW with learning rate 10^{-3} , weight decay 10^{-4} , and cosine annealing with 10-epoch linear warmup.

5. Downstream Evaluation

We now aim to understand whether the learned AM-FM embeddings encode meaningful information for a wide variety of sensing tasks.

5.1. Tasks and Evaluation Protocol

Tasks and Datasets. We evaluate on nine tasks spanning six categories of ambient perception applications. *Physiolog-*

cal sensing includes fall detection, identifying acute events from transient signal disruptions. *Activity understanding* covers human activity recognition (HAR) and motion source recognition (MSR, distinguishing human vs. non-human motion). *Spatial reasoning* comprises occupancy detection (presence/absence), localization (estimating position), and proximity estimation (distance to the sensor). *Biometrics* is represented by user identification (UID), distinguishing individuals from their characteristic motion patterns. *Fine-grained motion* includes gesture recognition, targeting short-duration micro-motions. *Spatial reconstruction* includes WiFi imaging, which reconstructs spatial structure from reflected signals. These tasks vary in temporal granularity (event vs. continuous vs. frame-level), spatial resolution (room-level vs. meter-level vs. pixel-level), and output complexity (binary vs. multi-class vs. dense), providing a comprehensive evaluation of representation quality.

We use three public benchmarks: CSI-Bench (Zhu et al., 2025a) (461 hours, 26 environments, 35 users, 16 device types), which covers a wide range of tasks collected in-the-wild; SignFi (Ma et al., 2018) for 276-class gesture recognition; and WiFiCam (Strohmayer et al., 2024) for spatial reconstruction.

Experiment Set-Up. We compare three adaptation strategies: *Bottleneck Adaptation (BA)* freezes the encoder and trains lightweight adapters with the task head; *Temporal Probe (TP)* freezes the encoder and trains only a temporal classifier; *Scratch* trains the encoder from random initialization. All use identical encoder structure, data splits, and training settings. We report AUROC with 95% bootstrap confidence intervals for classification tasks, and SSIM/PSNR for reconstruction.

5.2. Cross-Task Transfer Performance

Table 1 reports transfer results on nine downstream tasks using a *single* AM-FM backbone. With bottleneck adaptation, AM-FM exceeds 0.90 AUROC on all eight classification tasks, demonstrating broad transferability across physiological event sensing, activity understanding, spatial reasoning, and biometrics. Beyond classification, AM-FM also supports dense reconstruction: on WiFi imaging it achieves

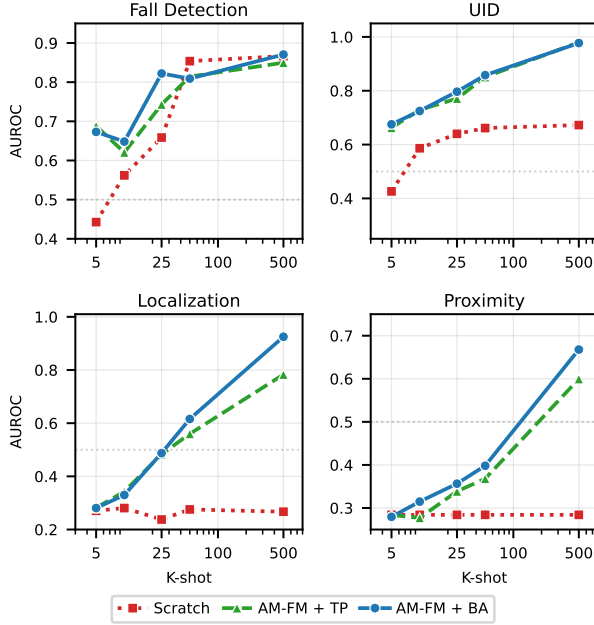


Figure 2. Cross-task transfer performance with small data sample sizes on four downstream tasks.

0.726 SSIM and 18.87 PSNR, indicating that pre-training preserves spatial structure needed for pixel-level prediction.

Comparing adaptation strategies clarifies what is already linearly accessible from the pre-trained space versus what requires task-specific recombination. Temporal probing is strong on User ID (0.996), Motion Source Recognition (0.992), Localization (0.990), Occupancy (0.989), Proximity (0.928), and HAR (0.915), and it surpasses bottleneck adaptation on User ID and Motion Source Recognition, suggesting these attributes are well-separated in the representation and benefit from a simpler readout. In contrast, Gesture Recognition improves sharply with bottleneck adaptation (0.634 \rightarrow 0.999), consistent with the increased complexity of 279-way fine-grained classification.

To isolate the contribution of pre-training, we also train the *same* architecture from random initialization under identical downstream protocols. While scratch training is strong on User ID (0.995) and Fall Detection (0.916), tasks that demand fine-grained discrimination or robustness to deployment variation (HAR, Localization, Motion Source, Occupancy, Proximity, Gesture) exhibit substantial gains with AM-FM. Overall, these results show that AM-FM provides a transferable inductive bias that enables one backbone to replace task-by-task model development.

5.3. Data Efficiency

To assess label efficiency in realistic deployments, we restrict supervision to $K \in \{5, 10, 25, 50, 500\}$ samples per

Table 2. Downstream performance (AUROC) across model scales.

Task	Small (2M)	Base (5M)	Large (12M)
Fall Detection	0.898	0.919	0.627
HAR	0.840	0.923	0.524
User ID	0.984	0.993	0.990
Localization	0.979	0.995	0.985
Motion Source	0.971	0.974	0.515
Occupancy	0.980	0.989	0.651
Proximity	0.901	0.936	0.496

class. Figure 2 shows that pre-training consistently improves performance in the low-data regime and approaches full-data performance as K increases. With bottleneck adaptation, Fall Detection reaches 0.822 AUROC at $K = 25$ and 0.809 at $K = 50$. User ID reaches 0.797 at $K = 25$ and 0.858 at $K = 50$. Localization increases from 0.488 at $K = 25$ to 0.616 at $K = 50$ and reaches 0.925 at $K = 500$.

The effect is most pronounced on tasks where supervised training struggles to generalize. For Localization, scratch training stays low at roughly 0.27 across all K values and remains far below AM-FM even with full supervision, with 0.631 from scratch versus 0.925 for AM-FM at $K = 500$. Proximity shows a similar pattern. These are not simply harder tasks; they are tasks that require invariances that are difficult to discover from limited labeled data collected in a narrow setting. Pre-training supplies these invariances by learning from broad unlabeled variation, yielding a deployment-relevant outcome. AM-FM turns objectives that are otherwise label-hungry into tasks that improve reliably with modest annotation effort.

5.4. Scaling Behavior

We evaluate model scaling by pre-training three variants under identical objectives and training pipelines: Small with 2M parameters, Base with 5M parameters as AM-FM, and Large with 12M parameters. We then adapt each model using the same bottleneck protocol on CSI-Bench. Table 2 shows that the Base model achieves the best overall transfer and improves over Small on most tasks. For example, HAR increases from 0.840 to 0.923, Proximity increases from 0.901 to 0.936, and Fall Detection increases from 0.898 to 0.919. The Small model remains competitive with less than half the parameters, offering an attractive trade-off for deployment.

The Large model degrades on several tasks, suggesting that with a fixed pre-training dataset (9.2 M samples), capacity must be matched to data scale; beyond an optimal size, additional parameters are not effectively utilized. This motivates future scaling via broader and longer CSI collection on more diverse setups to support larger models. This motivates future scaling via broader and longer CSI collection (more devices/environments) to support larger models.

Table 3. Inter-class distance in the representation space.

Task	Pre-trained	Random Init	Ratio
Fall Detection	3.61	0.25	14.4 \times
Localization	4.12	0.24	17.4 \times
Human ID	5.16	0.21	24.2 \times
Proximity	3.64	0.14	26.5 \times
HAR	1.57	0.03	52.0 \times
Motion Source	2.58	0.12	21.0 \times
Average	3.45	0.16	25.9 \times

5.5. Representation Quality

To probe why AM-FM transfers well, we quantify representation geometry using inter-class distance, defined as the mean Euclidean distance between class centroids. We compute this metric with up to 2,000 samples per task and compare pre-trained encoders against randomly initialized ones. Table 3 shows that pre-training produces much larger class separation, ranging from 14 to 52 times, with an average gain of 25.9 times, despite using no downstream labels. This structure explains the strong temporal probing results, since a simple readout can succeed when classes form well-separated clusters, and it also explains the few-shot behavior, since only a small number of labels is needed to place decision boundaries. Tasks with the largest separation gains also exhibit the largest transfer gaps, such as HAR with 52 times higher separation and AUROC improving from 0.527 to 0.923, and Proximity with 26.5 times higher separation and AUROC improving from 0.494 to 0.936.

5.6. Discussion

Figure 3 evaluates an ablation that adds standard SimCLR-style image augmentations on top of WiFi-tailored perturbations. The results show consistent degradation on tasks requiring fine-grained temporal discrimination: HAR drops from 0.923 to 0.561 and Proximity drops from 0.936 to 0.608. We also observe noticeable declines on binary detection: Occupancy decreases from 0.989 to 0.882 and Fall Detection decreases from 0.919 to 0.882. In contrast, spatial-signature tasks remain largely unchanged, with User ID increasing from 0.993 to 0.996 and Localization decreasing slightly from 0.995 to 0.994. These findings support a key design principle: CSI “spectrogram-like” inputs do not share the invariances of natural images, and naive cropping or distortion can remove the temporal windows or frequency components that encode sensing semantics. Effective pre-training therefore requires augmentations that mimic realistic wireless variation while preserving the signal’s physical meaning.

Pre-training provides the inductive bias needed for cross-environment robustness. The clearest value of AM-FM appears on tasks where supervised learning alone struggles

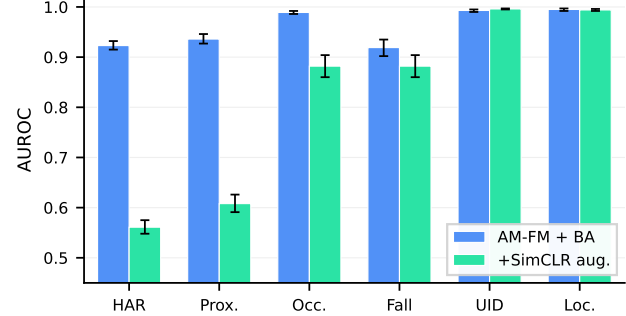


Figure 3. Effect of augmentation strategy on downstream performance.

to generalize. Scratch training yields low or near-chance performance on Proximity (0.494), HAR (0.527), Occupancy (0.566), Gesture (0.564), Motion Source (0.593), and Localization (0.631), whereas AM-FM achieves strong transfer on the same tasks (0.936, 0.923, 0.989, 0.999, 0.974, 0.995). Rather than attributing this solely to “more data,” these results indicate that unlabeled pre-training over diverse devices and environments teaches robust transformations that downstream supervision cannot easily discover from a narrow labeled dataset.

Adaptation strategy should follow task structure. Our results suggest a simple and reliable deployment recipe. When downstream labels align with the pre-trained structure, such as User ID and Motion Source Recognition, temporal probing can match or exceed heavier adaptation. This reflects strong linear separability and offers a lightweight option for constrained systems. When a task requires feature recombination, such as 279-way Gesture Recognition, bottleneck adaptation becomes essential. In practice, evaluating both strategies yields consistently strong performance while keeping a single unified backbone across tasks, reinforcing AM-FM as a practical foundation model rather than a collection of task-specific solutions.

6. Conclusion

We present AM-FM, the first foundation model for ambient intelligence via WiFi sensing. Pre-trained on 439 days of unlabeled CSI data spanning 20 device types and 11 environments, AM-FM transfers effectively across nine diverse tasks using a single unified backbone, exceeding 0.90 AUROC on all classification tasks. Few-shot experiments demonstrate practical data efficiency. Our results establish that the foundation model paradigm is applicable to ambient intelligence: domain-specific architectures and physics-aware objectives enable learning general-purpose representations from unlabeled data, replacing task-specific pipelines with a unified approach to privacy-preserving, always-on perception.

Impact Statement

This paper presents the first foundation model for ambient intelligent and sensing by using real and large dataset obtained from data commercially deployed worldwide. It represents the first step toward building a foundation model and validates significant performance improvements over various activities from existing works. Not only it demonstrates the promise in developing a universal ambient intelligent and sensing system, but also lay out a foundation toward realizing such a system to benefit humanity.

References

Abdelnasser, H., Harras, K. A., and Youssef, M. UbiBreathe: A ubiquitous non-invasive WiFi-based breathing estimator. In *Proceedings of the 16th ACM International Symposium on Mobile Ad Hoc Networking and Computing*, MobiHoc '15, pp. 277–286, New York, NY, USA, 2015a. Association for Computing Machinery.

Abdelnasser, H., Youssef, M., and Harras, K. A. WiGest: A ubiquitous WiFi-based gesture recognition system. In *2015 IEEE Conference on Computer Communications (INFOCOM)*, pp. 1472–1480, 2015b.

Ahmad, I., Ullah, A., and Choi, W. WiFi-based human sensing with deep learning: Recent advances, challenges, and opportunities. *IEEE Open Journal of the Communications Society*, 5:3595–3623, 2024.

Baevski, A., Zhou, H., Mohamed, A., and Auli, M. wav2vec 2.0: a framework for self-supervised learning of speech representations. In *Proceedings of the 34th International Conference on Neural Information Processing Systems*, NIPS '20, Red Hook, NY, USA, 2020. Curran Associates Inc.

Brunello, A., Montanari, A., Montoliu, R., Moreira, A., Saccomanno, N., Sansano-Sansano, E., and Torres-Sospedra, J. Time matters: Empirical insights into the limits and challenges of temporal generalization in CSI-based Wi-Fi sensing. *Internet of Things*, 32:101634, 2025.

Chen, T., Kornblith, S., Norouzi, M., and Hinton, G. A simple framework for contrastive learning of visual representations. ICML'20. JMLR.org, 2020.

Chu, Y., Cumanan, K., Sankarpandi, S. K., Smith, S., and Dobre, O. A. Deep learning-based fall detection using WiFi channel state information. *IEEE Access*, 11:83763–83780, 2023.

Guo, Z., Yuan, W., Gui, L., Sheng, B., and Xiao, F. Breath-Band: A fine-grained and robust respiration monitor system using WiFi signals. *ACM Trans. Sen. Netw.*, 19(4), May 2023.

He, K., Fan, H., Wu, Y., Xie, S., and Girshick, R. Momentum contrast for unsupervised visual representation learning. In *2020 IEEE/CVF Conference on Computer Vision and Pattern Recognition (CVPR)*, pp. 9726–9735, 2020.

He, K., Chen, X., Xie, S., Li, Y., Dollár, P., and Girshick, R. Masked Autoencoders Are Scalable Vision Learners. In *2022 IEEE/CVF Conference on Computer Vision and Pattern Recognition (CVPR)*, pp. 15979–15988, 2022.

Hu, Y., Zhu, G., Wang, W.-H., Wang, B., and Liu, K. J. R. What you need is a good CSI. In *Proceedings of the 30th Annual International Conference on Mobile Computing and Networking*, ACM MobiCom '24, pp. 1608–1610, New York, NY, USA, 2024. Association for Computing Machinery.

Kotaru, M., Joshi, K., Bharadia, D., and Katti, S. SpotFi: Decimeter level localization using WiFi. pp. 269–282, 2015.

Ma, Y., Zhou, G., Wang, S., Zhao, H., and Jung, W. SignFi: Sign language recognition using WiFi. *Proc. ACM Interact. Mob. Wearable Ubiquitous Technol.*, 2(1), March 2018.

Ma, Y., Zhou, G., and Wang, S. WiFi sensing with channel state information: A survey. *ACM Comput. Surv.*, 52(3), June 2019.

Miao, F., Huang, Y., Lu, Z., Ohtsuki, T., Gui, G., and Sari, H. Wi-Fi sensing techniques for human activity recognition: Brief survey, potential challenges, and research directions. *ACM Computing Survey*, 57(5), January 2025.

Radford, A., Kim, J. W., Hallacy, C., Ramesh, A., Goh, G., Agarwal, S., Sastry, G., Askell, A., Mishkin, P., Clark, J., Krueger, G., and Sutskever, I. Learning Transferable Visual Models From Natural Language Supervision. In *International Conference on Machine Learning*, 2021.

Radwan, A. Y., Yildirim, M., Hasanzadeh, N., Tabassum, H., and Valaei, S. A Tutorial-Cum-Survey on Self-Supervised Learning for Wi-Fi Sensing: Trends, Challenges, and Outlook. *IEEE Communications Surveys and Tutorials*, 28:2345–2376, 2026.

Strohmayer, J., Sterzinger, R., Stippel, C., and Kampel, M. Through-wall imaging based on WiFi channel state information. In *2024 IEEE International Conference on Image Processing (ICIP)*, pp. 4000–4006, 2024.

Su, W., Wang, C., Li, J., Yu, Z., and Jin, L. A novel feature extraction framework based on periodic features for human activity recognition using wearable sensor data. *Digital Signal Processing*, 168:105584, 2026.

Tao, Z., Wang, Z., Liu, Y., He, Y., and Wang, Y. Wireless perceptual space modeling method for cross-domain human activity recognition. *ACM Trans. Embed. Comput. Syst.*, 24(3), April 2025.

van der Maaten, L. and Hinton, G. E. Visualizing data using t-SNE. *Journal of Machine Learning Research*, 9: 2579–2605, 2008.

Wang, F., Zhang, T., Xi, W., Ding, H., Wang, G., Zhang, D., Cui, Y., Liu, F., Han, J., Xu, J., and Han, T. X. A survey on Wi-Fi sensing generalizability: Taxonomy, techniques, datasets, and future research prospects, 2025.

Wang, W., Liu, A. X., Shahzad, M., Ling, K., and Lu, S. Understanding and Modeling of WiFi Signal Based Human Activity Recognition. In *Proceedings of the 21st Annual International Conference on Mobile Computing and Networking*, MobiCom '15, pp. 65–76, New York, NY, USA, 2015. Association for Computing Machinery.

Wang, W., Wang, B., Hu, Y., Zhu, G., and Liu, K. J. R. Device-free room-level localization with WiFi utilizing spatial-frequency-time diversity. *IEEE Internet of Things Journal*, 11(21):35689–35698, 2024.

Wang, Z., Chen, S., Yang, W., and Xu, Y. Environment-independent Wi-Fi human activity recognition with adversarial network. In *ICASSP 2021 - 2021 IEEE International Conference on Acoustics, Speech and Signal Processing (ICASSP)*, pp. 3330–3334, 2021.

Xie, Y., Li, Z., and Li, M. Precise power delay profiling with commodity Wi-Fi. *IEEE Transactions on Mobile Computing*, 18(6):1342–1355, 2019.

Xu, H., Zhou, P., Tan, R., Li, M., and Shen, G. LIMU-BERT: Unleashing the Potential of Unlabeled Data for IMU Sensing Applications. In *Proceedings of the 19th ACM Conference on Embedded Networked Sensor Systems*, SenSys '21, pp. 220–233, New York, NY, USA, 2021. Association for Computing Machinery.

Zhang, F., Wu, C., Wang, B., Lai, H.-Q., Han, Y., and Liu, K. J. R. WiDetect: Robust motion detection with a statistical electromagnetic model. *Proc. ACM Interact. Mob. Wearable Ubiquitous Technol.*, 3(3), September 2019.

Zhang, F., Wu, C., Wang, B., Wu, M., Bugos, D., Zhang, H., and Liu, K. J. R. SMARS: Sleep monitoring via ambient radio signals. *IEEE Transactions on Mobile Computing*, 20(1):217–231, 2021.

Zhang, J., Tang, Z., Li, M., Fang, D., Nurmi, P., and Wang, Z. CrossSense: Towards cross-site and large-scale WiFi sensing. In *Proceedings of the 24th Annual International Conference on Mobile Computing and Networking*, MobiCom '18, pp. 305–320, New York, NY, USA, 2018. Association for Computing Machinery.

Zhao, L., Xiao, R., Liu, J., and Han, J. One is enough: Enabling one-shot device-free gesture recognition with COTS WiFi. In *IEEE INFOCOM 2024 - IEEE Conference on Computer Communications*, pp. 1231–1240, 2024.

Zheng, Y., Zhang, Y., Qian, K., Zhang, G., Liu, Y., Wu, C., and Yang, Z. Zero-effort cross-domain gesture recognition with Wi-Fi. *MobiSys '19*, pp. 313–325, New York, NY, USA, 2019. Association for Computing Machinery.

Zhou, R., Lu, X., Zhao, P., and Chen, J. Device-free presence detection and localization with SVM and CSI fingerprinting. *IEEE Sensors Journal*, 17(23):7990–7999, 2017.

Zhu, G., Hu, Y., Gao, W., Wang, W.-H., Wang, B., and Liu, K. J. R. CSI-Bench: A Large-Scale In-the-Wild Dataset for Multi-task WiFi Sensing. In *arXiv preprint arXiv:2505.21866*, 2025a.

Zhu, G., Wang, B., Gao, W., Hu, Y., Wu, C., and Ray Liu, K. J. SrcSense: Robust WiFi-based motion source recognition via signal-informed deep learning. *IEEE Journal of Selected Areas in Sensors*, 2:40–53, 2025b. doi: 10.1109/JSAS.2024.3517514.

A. Dataset Description

A.1. Pre-Training Dataset

The pre-training dataset was designed for large-scale self-supervised representation learning, without requiring any manual annotations. The CSI was collected continuously, 24/7, across diverse residential environments, capturing naturally occurring WiFi dynamics arising from everyday human activities, periods of inactivity, and environmental variations. IoT devices are distributed throughout participants' homes and operate under normal usage conditions, allowing the dataset to reflect realistic, in-the-wild sensing scenarios rather than segmented or scripted activities.

The resulting dataset spans 26 users, 20 IoT device types (33 devices in total), and 11 distinct residential environments, capturing heterogeneous WiFi sensing conditions across both commodity IoT deployments and dedicated sensing devices. In total, the corpus comprises over 439 days of continuous CSI recordings, amounting to approximately 20 TB of raw CSI data, 9,206,316 data samples, collected across the 2.4 GHz and 5 GHz bands with channel bandwidths of 20/40/80 MHz

A.2. Downstream Datasets

To evaluate the AM-FM foundation model, we use three public datasets spanning nine downstream tasks. We describe the data of each task in detail below.

Motion source recognition: This dataset captures motion patterns from humans, pets, robots, and fans in diverse indoor environments, including homes, townhouses, and offices. It involves 13 humans (ages 23–34), 11 pets, Roomba robots, and oscillating fans performing activities such as walking, sneaking, and simulated intrusion. CSI data are collected using NXP88W8997 2×2 devices at 100 Hz over 58 subcarriers. Each session lasts 3–8 minutes, with human motion optionally logged by users and non-human motion passively recorded. The dataset comprises approximately 150 k seconds of human motion, 2,000 minutes of pet activity, 1,000 minutes of robot activity, and 200 minutes of fan motion.

Fall detection: This dataset evaluates human fall recognition in real residential environments using commodity WiFi hardware. CSI is collected with synchronized video ground truth under varied hardware and environmental conditions. Data are recorded using NXP88W8997 2×2 802.11ac devices at 5.18 GHz, 40 MHz bandwidth, 100 Hz sampling rate (58 subcarriers), and ESP32-S3 devices at 2.4 GHz, 1×1 setup (64 subcarriers). nineteen participants performed walking, sitting, lying down, and falling across six indoor environments in both LoS and NLoS layouts, with ambient noise from ceiling fans to mimic real conditions. In total, the dataset contains 2,770 fall and 3,930 non-fall activities.

Localization: This dataset enables room-level user localization in typical households with both single- and multi-user activities. It includes data from eight users across six homes, with three rooms labeled per home. Eight device types (e.g., Echo, Google Nest, HomePod) operate on 2.4/5 GHz at 30–100 Hz with 20–80 MHz bandwidths. Users manually annotated room presence and co-occupancy during natural activities, resulting in 3,805 single-user and 3,257 multi-user samples across 6 environments.

User identification: This dataset captures user biometrics by distinguishing individuals based on their characteristic motion patterns. It includes data from six users collected using 5–7 IoT devices (e.g., Amazon Echo, Google Nest, Apple HomePod, and ESP32-based smart plugs) operating in the 2.4 and 5 GHz bands. Each user performs a set of activities including walking, running, sitting, and jumping. In total, the dataset contains ~6,000–7,000 samples per user.

Occupancy detection: This dataset consists of 24-hour CSI data collected from six households, capturing periods of human presence and absence. The data span six distinct environments, including three houses and three apartments. CSI is collected from 4–8 commercial IoT devices (e.g., Wiz light bulbs, Amazon Echo, Echo Show, and Google Home Mini) placed around each home and operating in the 2.4 and 5 GHz bands, with a sampling rate of 30 Hz. The dataset comprises approximately 150 minutes of human presence data and 150 minutes of empty-house data.

Proximity recognition: This dataset is designed for four-class distance estimation, with users positioned at different distances (0.5m, 1.5m, 2.5m, and 3.5m) from the device. Data was collected from six users across multiple distinct environments using diverse IoT hardware operating on both 2.4GHz and 5GHz frequencies at a 100Hz sampling rate. The dataset contains a total of 64,154 samples.

Human activity recognition: This dataset includes five human activities—walking, running, jumping, seated breathing, and waving—captured across diverse indoor environments and users. It contains data collected from six users in six distinct environments using IoT devices operating in the 2.4 and 5 GHz bands at a sampling rate of 100 Hz. The dataset comprises

approximately 5,000–6,000 samples per activity, with each activity lasting 3–6 minutes.

Gesture recognition: SignFi (Ma et al., 2018) is a publicly available WiFi sensing dataset for sign language recognition using CSI. The dataset captures wireless signal variations induced by 276 American Sign Language gestures encompassing head, arm, hand, and finger movements. Data was collected from five users across two environments: a laboratory and a home. Each user performed all 276 gestures with 20 repetitions in the lab and 10 in the home, yielding 5,520 lab instances and 2,760 home instances for a total of 8,280 samples. Each sample provides CSI measurements with dimensions of 200 time samples \times 30 subcarriers \times 3 transmit-receive antenna pairs, capturing both amplitude and phase information. SignFi presents challenges including high inter-class similarity, significant intra-class variability across users, and environmental variations.

WiFi imaging: The WiFiCam (Strohmayer et al., 2024) is multimodal dataset comprising temporally synchronized CSI and RGB images collected in indoor office environment. Data are recorded using ESP32-S3 based point-to-point transmitter receiver system operating at 2.4 GHz with 100 Hz sampling rate, while the images captured at 640 \times 480 resolution and 30 Hz sampling rate using and ESP32-S3 camera. The dataset contains ten-minute continuous human walking data.

B. Data Collection Protocol

B.1. Subjects and Scenarios

Our dataset includes CSI data collected from 26 participants aged 5–65 years across multiple residential environments, each with distinct household compositions. The participants comprise 8 adult males, 13 adult females, and 5 children, with heights ranging from 130 to 180 cm and body weights from 30 to 90 kg.

B.2. Devices and Hardware Diversity

To ensure comprehensive coverage of real-world IoT infrastructure, we select 20 commercial WiFi-enabled edge devices operating on both 2.4 GHz and 5 GHz bands with 20, 40, and 80 MHz bandwidths. The devices span major chipset vendors and range from low-cost smart plugs to high-performance routers and smart speakers. Before data collection, each device is validated with in-house CSI verification tool for signal consistency, sampling stability, and amplitude dynamics. Only devices meeting quality thresholds are deployed (Hu et al., 2024). All devices connect through an Asus GT-AX11000 router (Broadcom 4912 quad-core CPU at 2 GHz, 1 GB RAM). Table 4 summarizes their specifications.

Table 4. Summary of edge devices, WiFi chipsets, and specifications.

Device	Chipset	Model	Antenna	Bandwidth(MHz)	Band(GHz)
AmazonFireTVCube 2 gen	–	–	2x2	20/40	2.4 & 5
AmazonPlug	MediaTek	MT7697N	1x1	20	2.4
AmazonEchoPlus	MediaTek	MT8516	1x1	20/40/80	2.4 & 5
AmazonEchoShow 8	MediaTek	MT8183	1x1	20/40/80	2.4 & 5
AmazonEchoSpot	MediaTek	MT6625L	1x1	20/40	2.4 & 5
AmazonEchodot 2 gen	MediaTek	MT6625LN	1x1	20/40	2.4 & 5
AmazonEchodot 3 gen	MediaTek	MT7658CSN	1x1	20/40/80	2.4 & 5
GoogleHomeMini	Marvell	88W8887	1x1	20/40/80	2.4 & 5
GoogleNest	Qualcomm	IPQ4019	1x1	20/40	2.4 & 5
GoogleNestHub	Broadcom	BCM4345	1x1	20/40/80	2.4 & 5
WyzeCamera	Altobeam	ATBM6062	1x1	20	2.4
WyzePlug	Espressif	ESP8266/ESP8285	1x1	20	2.4
ESP32	Espressif	S3	1x1	20/40MHz	2.4
GoveePlug	Espressif	ESP8266/ESP8285	1x1	20	2.4
EightreePlug	Espressif	ESP8266/ESP8285	1x1	20	2.4
AppleHomePod	–	–	1x1	20/40	2.4G & 5G
BW16	RealTek	RTL8720DN	1x1	20/40	2.4 & 5
HealthPod	NXP	88W889	2x2	20/40/80	5
HexHome	Qualcomm	–	1x2	20/40	5
Lyra	Qualcomm	–	2x2	20/40/80	2.4 & 5

B.3. Environments

Data is collected across 11 distinct real-world environments, including studio apartments, multi-bedroom apartments, townhouses, and multi-floor single-family houses. These environments vary in layout complexity, room geometry, wall materials, and furniture density, introducing rich multipath and occlusion effects. To further diversify the CSI data, each environment features distinct device deployment configurations determined by user availability and spatial constraints. A summary of all environments is provided in Table 5.

Table 5. Summary of environments (XBXB indicates X bedrooms and X bathrooms; F: adult female, M: adult male, C: child).

Deployment Types	Type	Area (sqft)	Layout Type	Demography	Age	Height (cm) / Weight (kg)	# Floors
13	Single-family house	3800	Multi-room	1M, 1F, 2C	5–40	130–170 / 30–70	3
1	Apartment	576	Studio	1F	28	165–170 / 50–55	1
2	Apartment	714	1B1B	1M, 1F	31–32	160–175 / 50–80	1
1	Apartment	790	1B1B	1M, 1F	32	165–175 / 55–85	1
2	Apartment	1652	1B1B	1M, 1F	27–28	165–175 / 65–80	1
2	Single-family house	1904	Multi-room	2F	25–28	160–170 / 45–60	2
2	Apartment	830	1B1B	1F	28	160–165 / 45–55	1
2	Single-family house	2600	Multi-room	2M, 2F, 2C	3–65	130–170 / 30–90	3
2	Apartment	1200	2B2B	1M, 1F	25–30	160–175 / 50–80	1
2	Town House	1904	Multi-room	1M, 1F, 1C	5–42	130–180 / 30–85	3
1	Apartment	800	1B1B	1F	31	160–165 / 70–75	1

B.4. Continuous Data Recording

We design a scalable data acquisition framework to support continuous, 24/7 collection of WiFi CSI in real residential environments. The framework is designed to operate transparently within existing home networks, allowing CSI to be captured continuously during normal WiFi usage without modifying end devices or disrupting user behavior. This approach enables the construction of a large, naturally occurring CSI corpus spanning diverse households and deployment conditions.

CSI measurements are obtained through collaboration with router chipset vendors, who provide firmware-level access and vendor-specific utilities that expose CSI at the driver level. We implement custom acquisition software for both Linux- and FreeRTOS-based platforms that directly interface with WLAN kernel modules to stream CSI from all associated devices, which are periodically uploaded to cloud storage via AWS S3 APIs through Asus GT-AX11000 WiFi routers with adaptive upload scheduling to balance network load. All CSI files are indexed using UTC-based timestamps embedded at creation time, ensuring consistent temporal referencing across deployments and eliminating ambiguities caused by local time changes. This always-on data collection pipeline captures a wide range of real-world WiFi dynamics; the resulting CSI data are naturally unlabeled and used directly for self-supervised pre-training.

To support downstream analysis and investigation, we additionally provide users with an optional, lightweight Google Spreadsheet-based annotation interface (Figure 4) for coarse-grained activity logging. Users may voluntarily record events such as presence changes, sleep cycles, or room usage at their convenience, without requiring continuous interaction. These annotations are not required for data collection or pre-training, but enable post hoc analysis of CSI segments, such as examining whether observed signal variations correspond to user activities, environmental changes, or network instability. During post-processing, CSI segments corresponding to annotated intervals are retrieved and temporally refined using packet-level timestamps to generate labeled samples for evaluation and analysis.

C. CSI Quality Verification Tool and Filtering Pipeline

Raw CSI measurements obtained from commodity WiFi devices exhibit substantial variability arising from differences in chipset design, firmware behavior, antenna configuration, and deployment conditions. Typical failure modes include unstable sampling intervals, timestamp drift, gain fluctuations, and limited motion sensitivity. When such signals are indiscriminately included, these artifacts can bias self-supervised objectives and encourage shortcut learning, ultimately degrading representation quality and cross-domain generalization.

To construct a reliable pre-training dataset, we perform structured screening at the level of each *sensing device* prior to large-scale data ingestion. Rather than filtering individual segments during training, we use the following criteria to

Easy logging function	Start / End			
Info	Date	Tester	Start Time	End Time
Watching TV in living room	4/14/2025	U01	10:43:04	11:28:12
Cooking in kitchen	4/14/2025	U01	11:28:21	11:51:27
Eating in dining room	4/14/2025	U01	12:12:45	12:55:52
Watching TV in living room	4/14/2025	U01	13:26:50	13:59:56
Reading in office	4/14/2025	U01	14:00:53	16:04:00
Cooking in kitchen	4/14/2025	U01	16:07:18	15:10:25
Eating in dining room	4/14/2025	U01	17:11:15	18:04:23

Figure 4. Screenshot of the Google Spreadsheet-based annotation tool used by participants to record activities and timestamps during data collection.

determine whether a sensing device is suitable for inclusion in pre-training data collection.

C.1. Verification Criteria

Inspired by existing research in CSI qualification (Hu et al., 2024), we evaluate each sensing device along multiple complementary dimensions:

- **Timestamp consistency.** We analyze inter-packet intervals to estimate the effective sampling rate and its temporal stability. Sensing devices exhibiting sustained deviation from the nominal rate (30 Hz or 100 Hz), pronounced jitter, or long temporal gaps are excluded, since unreliable timing corrupts dynamics-sensitive representation learning.
- **Empty-scene stability.** For segments labeled as *empty* (no human motion), we assess whether CSI amplitude remains temporally stationary. Concretely, we monitor amplitude trajectories aggregated across subcarriers and reject sensing devices that exhibit abnormal fluctuations, drift, or bursty variations inconsistent with a static environment. This ensures a clean baseline for motion-sensitive learning.
- **Motion leakage under empty conditions.** We further screen empty segments for unintended motion signatures using lightweight motion statistics derived from amplitude dynamics. Sensing devices that repeatedly exhibit motion-like patterns in supposed empty scenes are removed, as they indicate interference or device instability that can introduce spurious correlations.
- **Motion sensitivity in active scenes.** For segments labeled as *motion*, we evaluate whether the sensing device is sufficiently sensitive to human movement. When motion occurs within an effective sensing range, the CSI amplitude is expected to exhibit a consistent deviation relative to the corresponding empty baseline. Sensing devices that fail to produce reliable motion-induced changes under these conditions are excluded, as they provide limited signal for learning motion-aware representations.

Only sensing devices that satisfy all criteria are retained for pre-training data collection and downstream evaluation.

C.2. Implementation

The above screening procedure is implemented as an offline device-selection stage prior to pre-training data collection, supported by a custom MATLAB-based diagnostic tool designed for rapid inspection and capability assessment of candidate sensing devices. Figure 5a and Fig 5b illustrate the diagnostic interface and representative visualizations used to assess timestamp stability and amplitude behavior across candidate sensing devices.

For each candidate device, short calibration sequences are recorded under both empty and motion conditions and processed by the tool to extract a small set of diagnostic statistics. These include temporal stability metrics computed from empty scenes as well as motion-related statistics from dynamic scenes.

The tool provides both quantitative summaries and visual diagnostics, including amplitude time series, time–subcarrier heatmaps, and stability/motion score traces, enabling efficient identification of unstable devices, interference-dominated

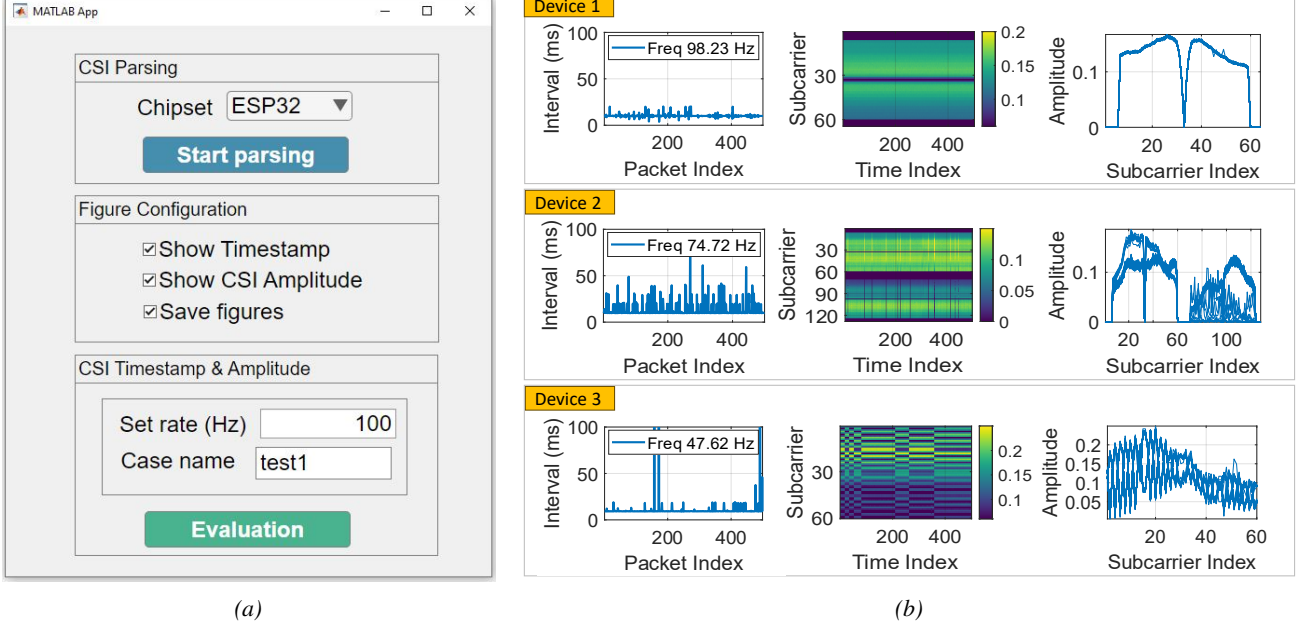


Figure 5. MATLAB-based CSI verification tool. (a) User interface for parsing and evaluating CSI data, supporting timestamp checks, amplitude analysis, and figure export to ensure data reliability in CSI-Bench. (b) Visualization of CSI quality from three devices, showing variations in sampling interval, time-subcarrier heatmap, and amplitude response. Device 1 exhibits the highest overall quality; Device 2 shows occasional outliers and packet loss; Device 3 exhibits severe packet loss and pronounced amplitude clustering artifacts.

channels, and devices with insufficient motion sensitivity. Device-specific statistics are compared against empirically determined thresholds derived from deployment-wide distributions.

The screening process is applied once per sensing device and does not require manual annotation or task-specific supervision. Links that fail any criterion are excluded from subsequent large-scale collection, while retained links are used to continuously acquire unlabeled CSI streams for pre-training.

This design enables scalable and reproducible construction of a high-quality pre-training dataset, while minimizing hardware-induced bias and ensuring that retained sensing devices exhibit both stable empty behavior and sufficient sensitivity to human motion.

C.3. CSI Pre-processing

CSI captures the frequency-domain characteristics of wireless channel propagation. We extract CSI amplitude from raw complex-valued measurements and apply a standardized pre-processing pipeline to ensure consistency between pre-training and downstream task evaluation. This section details the pre-processing steps, normalization methods, and data format standardization procedures.

C.3.1. RAW CSI DATA EXTRACTION

The foundation model operates on CSI amplitude data extracted from IEEE 802.11n/ac WiFi packets. Raw CSI measurements are complex-valued and represent the channel frequency response across OFDM subcarriers:

$$H(f_k) = |H(f_k)|e^{j\phi(f_k)} \quad (10)$$

where $|H(f_k)|$ is the amplitude and $\phi(f_k)$ is the phase at subcarrier frequency f_k . We retain only the amplitude component for the foundation model:

$$A_k = |H(f_k)| \quad (11)$$

The decision to use amplitude-only processing is motivated by several considerations. First, phase measurements are highly sensitive to carrier frequency offset, sampling clock offset, and packet detection timing—all of which vary substantially

across different WiFi hardware. Amplitude, by contrast, provides more stable and hardware-invariant representations. Second, amplitude is inherently more robust to multipath-induced rapid phase variations that introduce noise in practical deployments. Finally, prior work in WiFi sensing has empirically demonstrated that amplitude-based representations achieve comparable or superior performance to complex-valued representations for activity recognition tasks, while being substantially easier to process and generalize across devices.

C.3.2. DATA FORMAT STANDARDIZATION

CSI data from different sources exhibit varying tensor layouts. Our pipeline handles multiple input formats and standardizes all data to a unified representation suitable for the transformer encoder.

Table 6 summarizes the input formats supported by our preprocessing pipeline.

Table 6. Supported CSI Input Formats

Format	Shape	Description	Example
Downstream Task	$(F, T, 1)$	Single sample per file	$(64, 500, 1)$
Pre-training Batch	(N, T, F)	Multiple samples per file	$(1456, 500, 56)$
Standard 2D	(T, F)	Direct time-frequency matrix	$(500, 112)$

Here N denotes the number of samples, T the temporal dimension, and F the frequency (subcarrier) dimension. The preprocessing pipeline automatically detects the input format based on tensor dimensions. Two-dimensional tensors of shape (T, F) are used directly as time-frequency representations. Three-dimensional tensors with a trailing singleton dimension $(F, T, 1)$ are transposed to (T, F) format. Batch tensors of shape (N, T, F) with $T = 500$ are unpacked into individual samples.

All data is converted to the canonical format $\mathbf{X} \in \mathbb{R}^{1 \times T_{\text{target}} \times F_{\text{target}}}$, where the single channel contains amplitude information, $T_{\text{target}} = 500$ time steps, and $F_{\text{target}} = 112$ frequency bins corresponding to the maximum number of OFDM subcarriers across supported WiFi configurations.

C.3.3. PRE-PROCESSING PIPELINE

The pre-processing pipeline applies a strict sequence of operations to ensure consistency between pre-training and downstream evaluation. The order of operations is critical: padding must occur before normalization to match the statistics computed during pre-training.

Step 1: Shape Transformation. The input tensor is first converted to (T, F) format using format-specific transformations. Two-dimensional inputs pass through unchanged, three-dimensional inputs with trailing singleton dimensions undergo squeeze and transpose operations, and batch tensors are indexed to extract individual samples.

Step 2: Zero Padding. Dimensions are standardized to the target shape using zero padding:

$$\mathbf{X}_{\text{padded}}[t, f] = \begin{cases} \mathbf{X}[t, f] & \text{if } t < T_{\text{input}} \text{ and } f < F_{\text{input}} \\ 0 & \text{otherwise} \end{cases} \quad (12)$$

The temporal dimension is padded or truncated to $T_{\text{target}} = 500$, and the frequency dimension is padded or truncated to $F_{\text{target}} = 112$.

Step 3: Normalization. Sample-wise min-max normalization is applied to the padded tensor:

$$\mathbf{X}_{\text{norm}} = \frac{\mathbf{X}_{\text{padded}} - \min(\mathbf{X}_{\text{padded}})}{\max(\mathbf{X}_{\text{padded}}) - \min(\mathbf{X}_{\text{padded}}) + \epsilon} \quad (13)$$

where $\epsilon = 10^{-8}$ prevents division by zero. This operation scales all values to the range $[0, 1]$.

Step 4: Channel Dimension. A leading channel dimension is added to produce the final output:

$$\mathbf{X}_{\text{final}} = \text{unsqueeze}(\mathbf{X}_{\text{norm}}, 0) \in \mathbb{R}^{1 \times 500 \times 112} \quad (14)$$

The Pad → Normalize ordering is essential for consistency between pre-training and downstream evaluation. Reversing this order would produce different normalization statistics because min-max normalization computed on the original data excludes padded zeros, and adding zeros after normalization would alter the effective value distribution. Since pre-training uses the Pad → Normalize order, downstream evaluation must follow the same sequence to ensure feature compatibility with the pre-trained encoder.

C.3.4. NORMALIZATION METHODS

We support multiple normalization strategies, with min-max normalization serving as the default for both pre-training and downstream tasks. Min-max normalization is preferred for several reasons. The bounded output range prevents extreme activations that could destabilize training. The transformation preserves relative amplitude variations across the spectrogram, which encode important information about signal propagation and human activity. The approach is hardware-agnostic, accommodating different WiFi chipsets that may have different automatic gain control settings. Finally, bounded normalization to $[0, 1]$ is consistent with typical image preprocessing pipelines used in vision transformers, facilitating transfer of architectural insights from the computer vision literature.

D. Pre-training Details

D.1. Foundation Model Backbone

The input CSI spectrogram $\mathbf{X} \in \mathbb{R}^{1 \times T \times F}$ (where T is the time dimension and F is the frequency/subcarrier dimension) is first processed by an adaptive downsampling encoder that learns to compress the frequency dimension via cross-attention. The encoder operates with a single input channel, using 8 intermediate channels and 16 output channels. We employ $F_{\text{out}} = 10$ learnable query vectors, each of dimension $c_{\text{mid}} = 8$, to attend over the input frequency bins. The encoder computes attention scores between learnable queries and input frequency bins. The flattened features are projected and processed through a transformer encoder with learned relative position bias. Table 7 summarizes the architectural configurations across model scales.

Table 7. Transformer Encoder Hyperparameters

Hyperparameter	F1 Model	Small Model	Large Model
Embedding dimension (d_{model})	256	512	768
Encoder layers	6	8	12
Attention heads	8	8	12
Feed-forward dimension	512	1024	2048
Dropout	0.1	0.1	0.1
Max sequence length	512	512	512

D.1.1. PRE-TRAINING OBJECTIVES

The backbone is pre-trained with three joint objectives specifically designed for WiFi CSI data.

We employ a SimCLR-style contrastive learning framework adapted for the unique characteristics of WiFi CSI data. Unlike natural images, CSI spectrograms exhibit strong temporal correlations, frequency-domain structure from multipath propagation, and sensitivity to environmental dynamics. Our augmentation pipeline is specifically designed to preserve semantic content while creating diverse views.

Tables 8 details the signal-domain augmentations.

We employ a masked channel modeling (MCM) objective that reconstructs masked portions of the CSI spectrogram. This objective is specifically designed to capture the spatial-temporal-frequency structure unique to WiFi channel measurements. The design is motivated by three considerations: (1) *Multipath Structure*—WiFi CSI encodes multipath propagation where

Table 8. Signal-Domain Augmentations

Augmentation	Parameters	Rationale
Gaussian Noise	$\sigma = 0.002$	Simulates thermal noise and receiver imperfections
Amplitude Modulation	factor = 0.02	Models path loss variations and fading
Phase Shift	max_shift = 0.02	Simulates carrier frequency offset and timing errors
Temporal Shift	max_steps = 2	Models asynchronous sampling across devices
Frequency Perturbation	max = 0.008	Simulates frequency-selective fading

different frequency subcarriers experience correlated but distinct phase rotations; (2) *Temporal Dynamics*—human activities create time-varying signatures in CSI; and (3) *Cross-Domain Invariance*—masking entire rows and columns helps learn representations robust to missing or corrupted subcarriers.

Physics-Informed Auxiliary Task: Autocorrelation Function Prediction. We incorporate a physics-informed auxiliary objective based on the Autocorrelation Function (ACF) of the CSI signal power time series. This design is inspired by the theoretical foundations of acoustic and RF sensing, particularly the relationship between signal statistics and physical phenomena.

The ACF auxiliary task is motivated by several factors: (1) *Doppler Signature Encoding*—the ACF captures Doppler shifts induced by human motion; (2) *Motion Pattern Discrimination*—following the theoretical framework in SrcSense (Zhu et al., 2025b), the ACF encodes temporal structure of activity-induced signal variations; (3) *Hardware-Invariant Features*—the ACF is robust to hardware-specific gain variations; and (4) *Temporal Scale Information*—the decay rate reveals characteristic time scales of activities.

D.1.2. PRE-TRAINING INFRASTRUCTURE

Pre-training is conducted on 8 NVIDIA A100 40GB GPUs (AWS P4D.24xlarge instances) using PyTorch Distributed Data Parallel (DDP) with the NCCL backend. We employ mixed precision training (FP16/BF16) and gradient checkpointing to maximize memory efficiency. The total batch size is 80 samples (10 per GPU). We use the AdamW optimizer with a learning rate of 5×10^{-5} and cosine annealing schedule over 100 epochs. Training data is staged from FSx to local NVMe storage via parallel rclone transfers to minimize I/O bottlenecks.

D.2. Downstream Task Adaptation

D.2.1. TEMPORAL PROBING

Temporal probing freezes all encoder parameters and trains only the temporal classifier, testing whether pre-trained representations are separable without encoder adaptation.

D.2.2. BOTTLENECK ADAPTATION

For each linear layer in the transformer encoder, we add a parallel bottleneck path:

$$\mathbf{y} = \mathbf{W}_{\text{base}}\mathbf{x} + \mathbf{W}_{\text{up}} \cdot \sigma(\mathbf{W}_{\text{down}}\mathbf{x}), \quad (15)$$

where \mathbf{W}_{base} is frozen, $\mathbf{W}_{\text{down}} \in \mathbb{R}^{192 \times d_{\text{in}}}$ projects to the bottleneck, and $\mathbf{W}_{\text{up}} \in \mathbb{R}^{d_{\text{out}} \times 192}$ projects back with GELU activation. Dropout of 0.03 is applied within the adapter. The up-projection is zero-initialized so adapters act as identity at initialization.

D.2.3. WiFi-TO-IMAGE ADAPTATION

For the WiFi-imaging downstream task, we adapt the architecture by replacing the original encoder introduced in WiFi-Cam (Strohmayer et al., 2024) with our pre-trained AM-FM model and introducing a lightweight output adapter that maps the AM-FM backbone’s embedding dimension to the target dimension required by the image generation pipeline. During training, we employ bottleneck adaptation to fine-tune the AM-FM model.

Table 9. Test-set performance across downstream tasks (model: F1). AUROC is reported with 95% CI. FAR denotes false alarm rate.

Task	Method	AUROC	95% CI	Accuracy	F1	FAR
Fall Detection	Scratch	0.916	(0.899, 0.932)	0.827	0.844	0.117
	AM-FM + TP	0.873	(0.851, 0.893)	0.801	0.833	0.252
	AM-FM + BA	0.919	(0.902, 0.935)	0.834	0.852	0.125
Human Activity Recognition	Scratch	0.527	(0.513, 0.541)	0.520	0.137	0.200
	AM-FM + TP	0.915	(0.906, 0.922)	0.765	0.685	0.072
	AM-FM + BA	0.923	(0.915, 0.932)	0.800	0.729	0.059
User Identification	Scratch	0.995	(0.993, 0.997)	0.943	0.937	0.014
	AM-FM + TP	0.996	(0.994, 0.997)	0.933	0.932	0.018
	AM-FM + BA	0.993	(0.990, 0.995)	0.936	0.936	0.017
Localization	Scratch	0.631	(0.606, 0.653)	0.273	0.128	0.162
	AM-FM + TP	0.990	(0.986, 0.994)	0.914	0.899	0.019
	AM-FM + BA	0.995	(0.992, 0.997)	0.938	0.916	0.014
Motion Source Recognition	Scratch	0.593	(0.581, 0.606)	0.522	0.273	0.217
	AM-FM + TP	0.992	(0.991, 0.993)	0.936	0.920	0.027
	AM-FM + BA	0.974	(0.970, 0.977)	0.886	0.842	0.049
Occupancy Detection	Scratch	0.566	(0.544, 0.587)	0.506	0.021	0.002
	AM-FM + TP	0.989	(0.985, 0.992)	0.955	0.955	0.048
	AM-FM + BA	0.989	(0.986, 0.992)	0.958	0.958	0.043
Proximity Recognition	Scratch	0.494	(0.477, 0.510)	0.284	0.111	0.250
	AM-FM + TP	0.928	(0.919, 0.938)	0.749	0.752	0.085
	AM-FM + BA	0.936	(0.927, 0.946)	0.796	0.799	0.069

D.3. Training Configuration

We use largely consistent training hyperparameters for both temporal probing and bottleneck adaptation to ensure a fair comparison. Both methods are optimized using AdamW with an initial learning rate of 0.001 and a weight decay of 1e-4. Training is performed for up to 100 epochs with early stopping based on validation performance (patience of 10 epochs). Gradient norms are clipped to 1.0, and a cosine annealing learning rate scheduler is applied, with the minimum learning rate set to 1% of the initial value. Cross-entropy loss is used for all downstream classification tasks. The main difference lies in batch size: temporal probing uses a batch size of 64, while bottleneck adaptation uses smaller batches (16–32) due to higher memory consumption during partial fine-tuning.

D.4. Few-Shot Learning Configuration

For few-shot evaluation, we sample $k \in \{5, 10, 25, 50, 100, 500, 1000\}$ examples per class from the training set. Sampling is stratified by class label to ensure balanced representation across all categories. We report results averaged over multiple random seeds to ensure statistical reliability.

E. Detailed Results

E.1. Cross-Task Transfer Results

Table 9 provides cross-task transfer performance on the test split for a single backbone. Overall, pretraining yields strong transfer across heterogeneous sensing objectives, with *Bottleneck Adaptation* achieving consistently high AUROC and low false alarms on most tasks.

High transfer on spatial reasoning and presence sensing. Localization transfers exceptionally well: Bottleneck Adaptation reaches 0.995 AUROC with 0.938 accuracy, 0.916 F1, and 0.014 FAR. Occupancy Detection is similarly strong (0.989 AUROC), with 0.958 accuracy / 0.958 F1 and 0.043 FAR. Proximity Recognition also transfers well, reaching 0.936 AUROC with improved thresholded performance (0.796 accuracy, 0.799 F1) and 0.069 FAR.

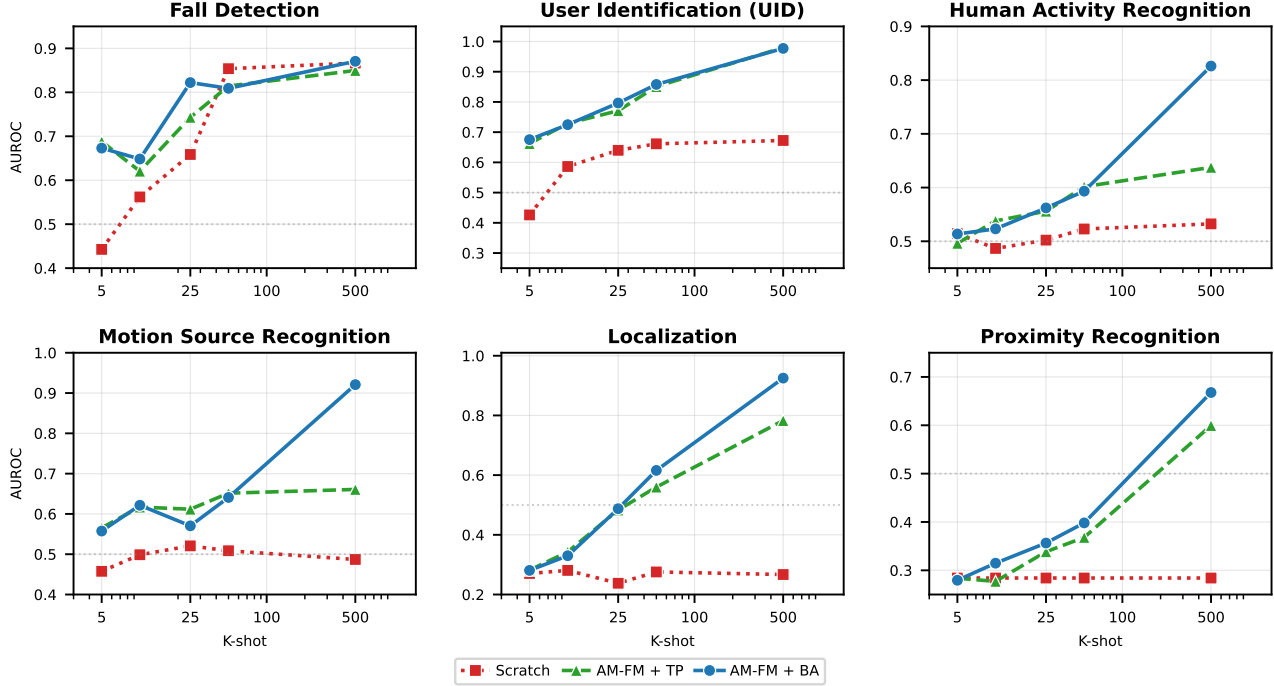


Figure 6. Enter Caption

Strong activity understanding with modest adaptation. For HAR, Bottleneck Adaptation improves both ranking and decision metrics, reaching 0.923 AUROC and 0.729 F1 with 0.059 FAR. Motion Source Recognition achieves the highest AUROC with Temporal Probe (0.992) and strong decision metrics (0.936 accuracy, 0.920 F1, 0.027 FAR), while Bottleneck Adaptation maintains high performance (0.974 AUROC) with a slight FAR increase (0.049).

Biometrics and event sensing. User identification is near-saturated across all adaptation strategies, with $\text{AUROC} \geq 0.993$ and very low FAR (≤ 0.018). For Fall Detection, Bottleneck Adaptation slightly improves AUROC over Scratch (0.919 vs. 0.916) with comparable thresholded performance (0.852 F1) and low FAR (0.125).

Scratch vs. adaptation. Training from Scratch underperforms on most tasks, with particularly large gaps on HAR (0.527 AUROC, 0.137 F1), Localization (0.631 AUROC, 0.128 F1), and Proximity (0.494 AUROC, 0.111 F1). In contrast, temporal probing already yields strong transfer on several tasks (e.g., Localization 0.990 AUROC; Motion Source Recognition 0.992 AUROC), while Bottleneck Adaptation provides the best or most consistent improvements in thresholded metrics (e.g., HAR and Proximity) and maintains low false alarm rates.

E.2. Data Efficiency Evaluation

We evaluate label efficiency by varying the number of labeled training examples per class ($K \in \{5, 10, 25, 50, 500\}$) and comparing (i) training from scratch, (ii) temporal probing, and (iii) bottleneck adaptation. Across tasks, pre-training yields clear gains in the low-shot regime, with bottleneck adaptation typically providing the strongest improvements as K grows.

Figure 6 shows that on *Fall Detection*, transfer is already effective at very small K : at $K=5$, temporal probing and bottleneck adaptation achieve 0.688 and 0.673 AUROC, compared to 0.443 when training from scratch. Gains remain consistent as more labels become available, reaching 0.850–0.871 AUROC at $K=500$ (vs. 0.867 from scratch). On *Human ID*, pre-training substantially improves data efficiency: at $K=50$, temporal probing and bottleneck adaptation reach 0.851/0.858 (vs. 0.661 from scratch), and at $K=500$ both methods approach near-saturated performance (0.980/0.977) while training from scratch remains at 0.673.

For multi-class activity tasks, pre-training is particularly beneficial at moderate and larger K . On *HAR*, performance improves from 0.523 (scratch) to 0.602 (temporal probe) at $K=50$, and bottleneck adaptation further scales to 0.826 at

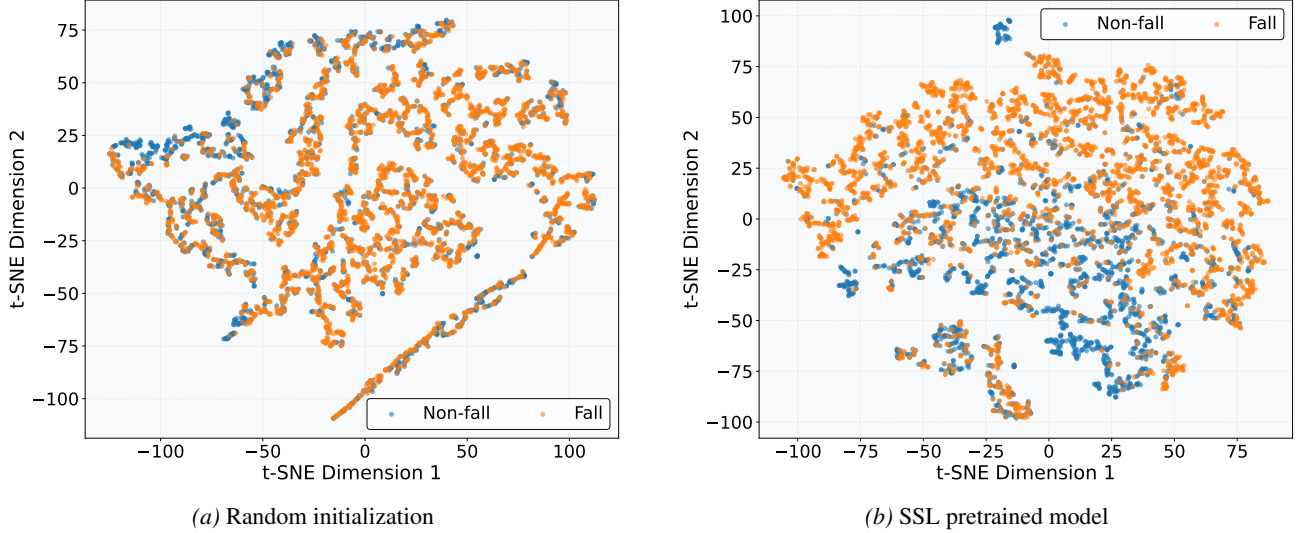


Figure 7. t-SNE visualization of learned representations for fall detection. (a) Random initialization shows overlapping clusters with poor class separation, indicating the model has not learned meaningful features. (b) SSL pretrained model demonstrates separation between fall and non-fall classes, revealing that self-supervised pretraining learns discriminative representations beneficial for downstream tasks.

$K=500$ (vs. 0.532 from scratch). On *Motion Source Recognition*, bottleneck adaptation provides the largest jump at $K=500$ (0.921 vs. 0.661 temporal probe and 0.487 scratch), indicating that fine-tuning a small number of task-specific parameters can effectively leverage the pre-trained representation when sufficient labels are available.

Spatial tasks show the strongest data-efficiency gains under bottleneck adaptation. For *Localization*, training from scratch remains near chance across all K (0.238–0.281 and 0.267 at $K=500$), whereas pre-training enables rapid improvement: temporal probing reaches 0.783 and bottleneck adaptation reaches 0.925 at $K=500$. For *Proximity*, transfer also improves steadily with K : at $K=500$, bottleneck adaptation achieves 0.668 AUROC compared to 0.600 for temporal probing and 0.284 from scratch, while low-shot settings remain challenging for all methods.

Overall, these few-shot results show that a single pre-trained backbone can achieve strong performance with limited labels, and that bottleneck adaptation generally offers the best scaling with additional supervision, especially on multi-class and spatial reasoning tasks.

E.3. Representation Analysis

To evaluate the quality of learned representations, we employ t-distributed Stochastic Neighbor Embedding (t-SNE) (van der Maaten & Hinton, 2008), a widely-used dimensionality reduction technique that projects high-dimensional feature embeddings into a two dimensional space while preserving local neighborhood structures. t-SNE visualization provides intuitive insights into how well the model separates different classes in the learned representation space. Well-separated clusters indicate that the model has learned discriminative features that capture class-specific patterns, while overlapping clusters suggest poor feature learning. We compare the quality of the representation between randomly initialized models and SSL pretrained models to demonstrate the effectiveness of pretraining.

Figure 7 illustrates the effectiveness of SSL pretraining for fall detection. The t-SNE embeddings in Figure 7a show that randomly initialized models produce highly overlapping clusters, where fall and non-fall samples are mixed together, demonstrating the lack of meaningful feature representation. In contrast, Figure 7b reveals that the SSL pretrained model achieves substantially better class separation, with fall and non-fall samples forming distinct clusters in the embedding space. This clear separation indicates that the pretrained model has learned discriminative features during self-supervised pretraining that effectively capture the essential patterns that distinguish fall events from non-fall activities. The improved separability in the embedding space directly translates to better classification performance, validating the value of SSL pretraining for learning robust representations even without labeled data.

Figure 9 presents the t-SNE visualization comparing representation quality for the localization task. In Figure 8a, the randomly initialized model produces severely entangled embeddings where all data points of the six classes overlap

Figure 8. Cross-task transfer performance with small numbers of samples.

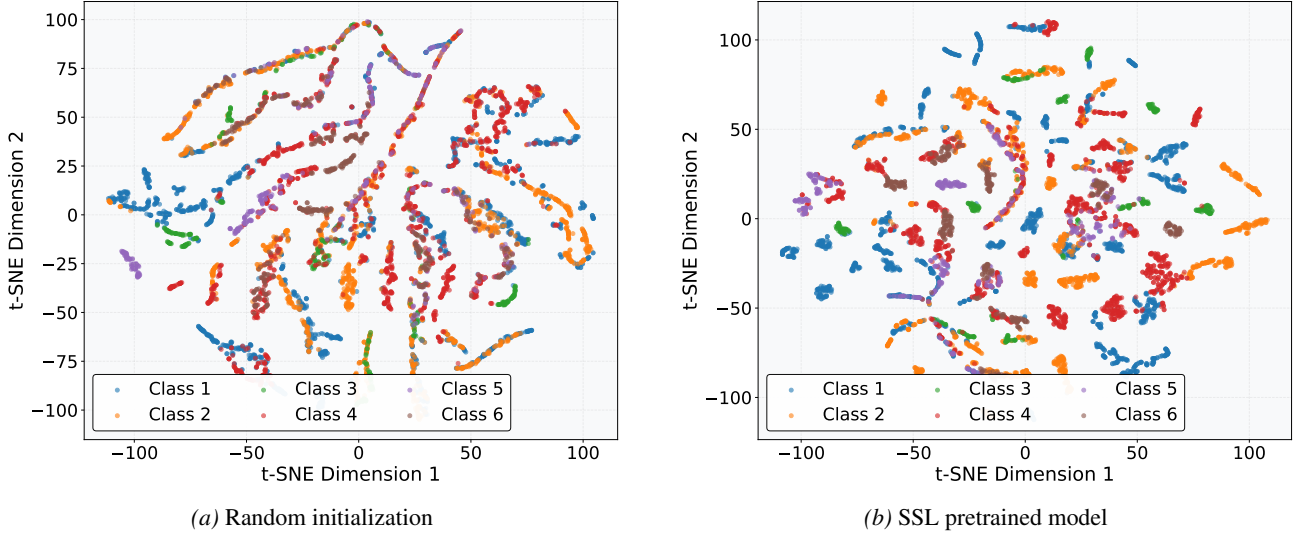


Figure 9. t-SNE visualization of learned representations for localization. (a) Random initialization exhibits highly overlapping clusters across all six classes, with no discernible boundaries between different locations, indicating the absence of meaningful spatial features. (b) SSL pretrained model shows improved cluster formation with reduced inter-class overlap, demonstrating that self-supervised pretraining captures spatial patterns that facilitate location-specific classification.

extensively, forming intertwined patterns with no clear spatial structure. This chaotic distribution indicates that, without proper feature learning, the model cannot distinguish between different locations based on the patterns of wireless signals.

Conversely, Figure 8b demonstrates that the SSL pretrained model achieves notably better separation in the embedding space. While some inter-class overlap persists due to the inherent complexity of the localization task, the pretrained model forms more cohesive class-specific clusters with clearer boundaries. This improvement suggests that SSL pretraining enables the model to learn location-dependent signal characteristics such as propagation patterns, multipath effects, and signal strength variations that are crucial for distinguishing between different locations. The enhanced separability in the pretrained embeddings translates to improved localization accuracy, validating the effectiveness of SSL pretraining for learning robust spatial representations from unlabeled wireless sensing data.